Summary of Content

Section 1. Analysis of Anti-Crossing between IX_D and X_A

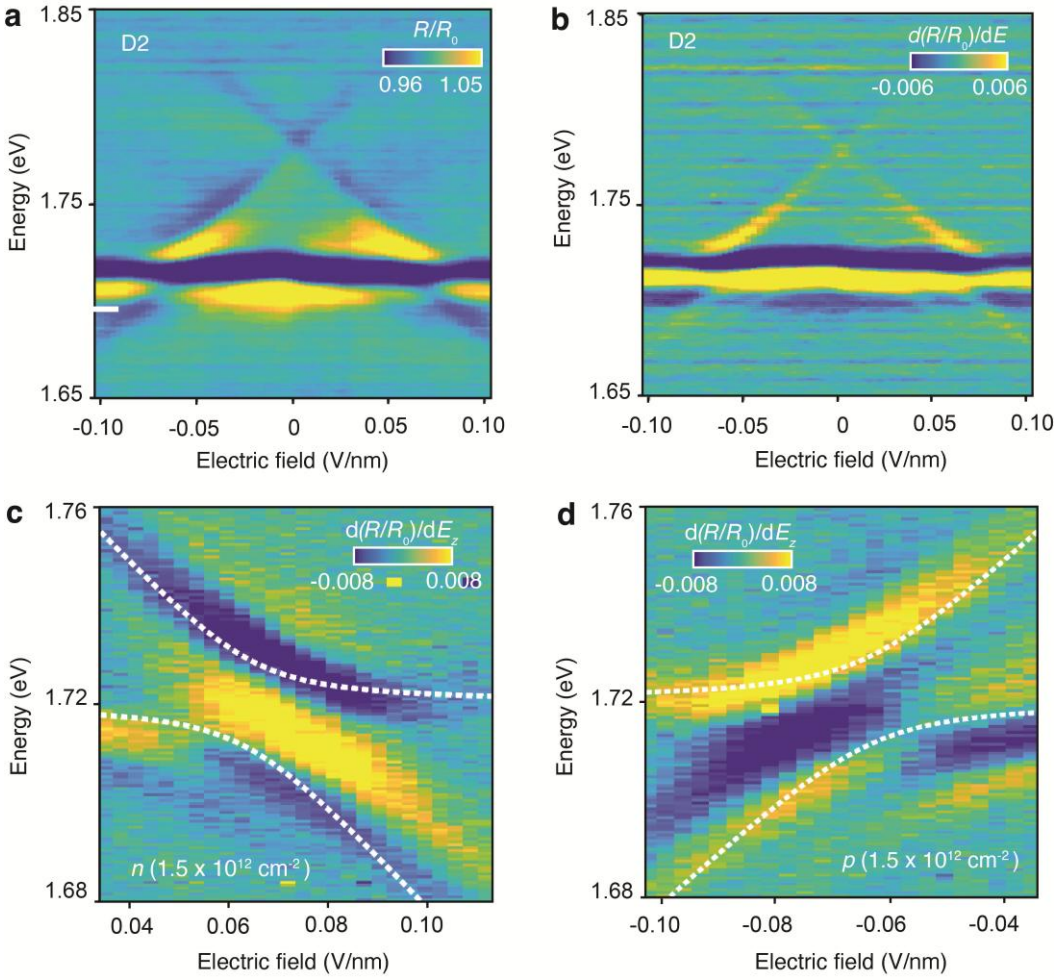

Figure S1 Anti-crossing between IX_D and X_A for various doping concentrations in device D2. **a,** Reflectance spectra (R/R_0) as a function of the electric field in the intrinsic regime. **b,** Differential reflectance spectrum (d(R/R_0)/dE) as a function of the electric field. The anti-crossing takes place at ~0.05 V/nm, consistent with device D1. **c, d,** Zoom-in view of the differential reflectance under electron (**c**) and hole(**d**) doped with an applied electric field. The white dashed lines represent the energies fitted with a two-level model. The fitted coupling strength **W** for electron and hole-doped side is around ~10 meV and comparable with that in intrinsic trilayer.

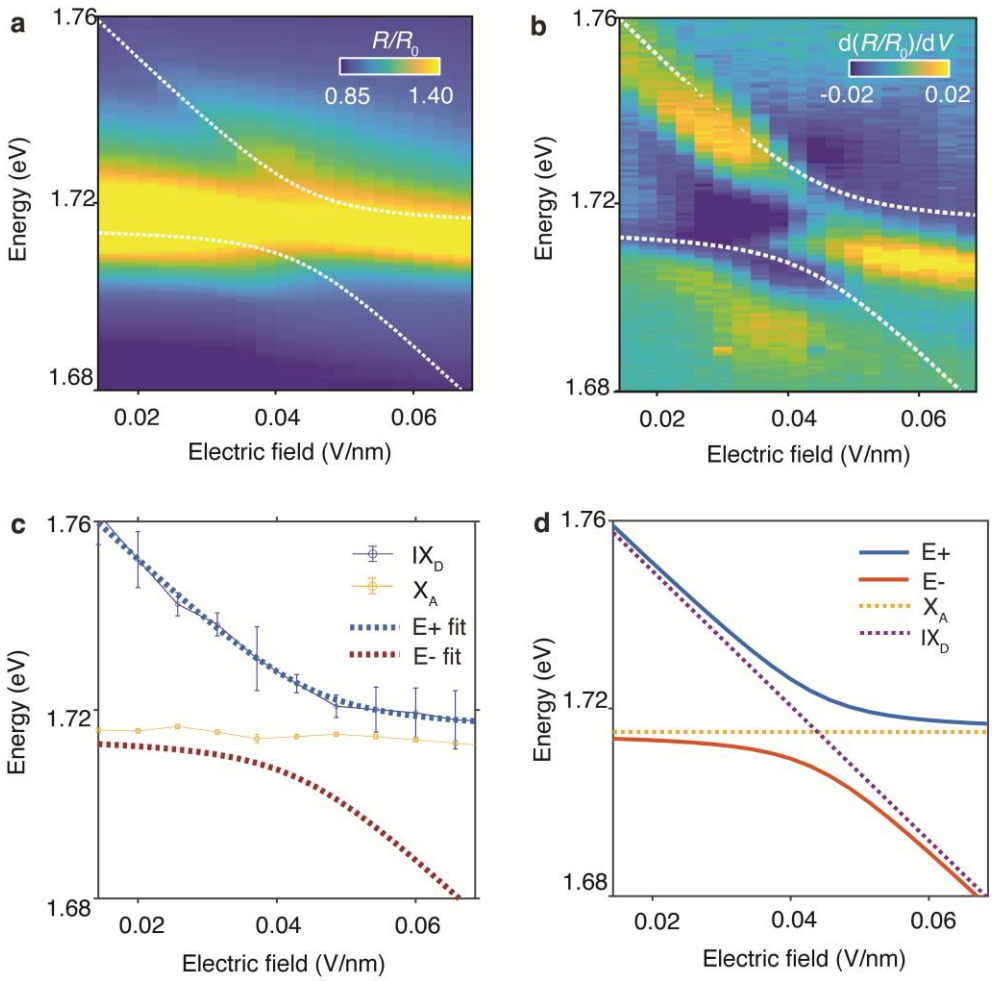

Figure S2 Analysis of anti-crossing between IX_D and X_A in device D1. a, Reflectance spectra (R/R_0) as a function of the electric field near the anti-crossing region. **b,** Voltage derivative of reflectance spectra, d(R/R_0)/dV. The white dashed lines in (a) and (b) represent the energies fitted with a two-level model. **c, d,** We study the anti-crossing between the IX_D and X_A based on a two-level system with a Hamiltonian:

$$H = \begin{pmatrix} E1 & W \\ W & E2 \end{pmatrix}$$

where E_1 and E_2 are the unperturbed energies of the IX_D and X_A, respectively, and W is the coupling strength. The new eigenvalues can be expressed as:

$$E_{\pm} = \frac{1}{2}(E_1 + E_2) \pm \frac{1}{2}\sqrt{(E_1 - E_2)^2 + 4|W|^2}$$

where $E_{\pm}$ correspond to the energies of the two branches. In (**c**), we extract the peak positions $E_{\pm}$ by fitting the reflectance spectra with the Lorentzian function. The error bars represent the variance of fitting peak energy. We then set E_2 to be 1.715eV, which is the mean energy of X_A, and keep it as a constant. E_1 is calculated based on the IX_D energy at zero electric fields and the stark shift. The stark shift slope k is estimated to be -1.436 eV/V in this particular device. The fitted anti-crossing is shown in (**d**) with a fitting parameter of $W = 10 \pm 2\ meV$.

Section 2. Doping-dependent photoluminescence map of trilayer WSe_2

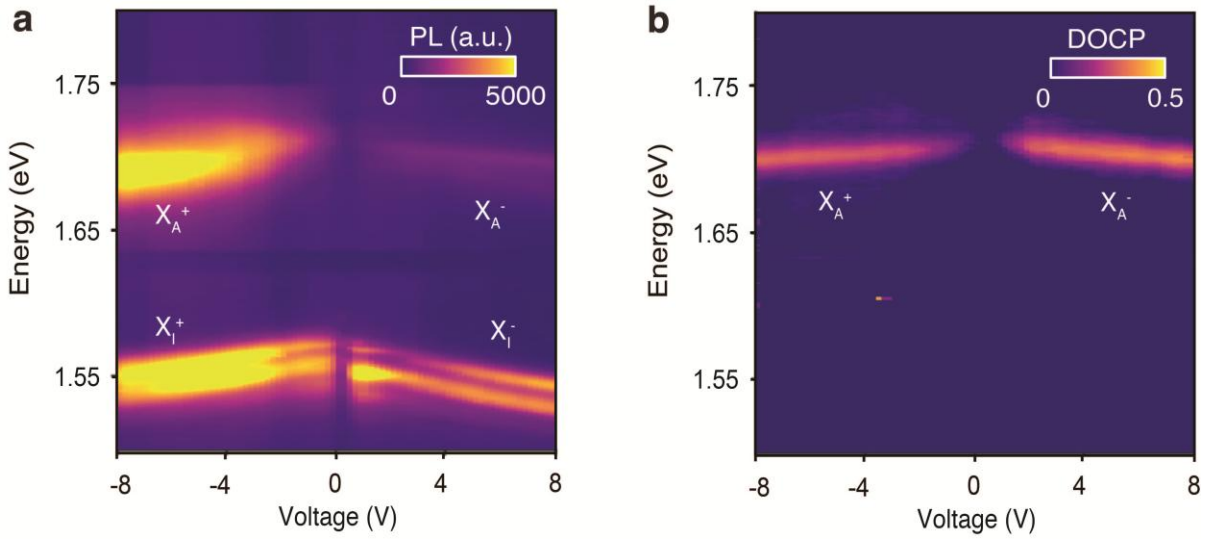

Figure S3 a, Doping-dependent photoluminescence of the trilayer WSe_2 at $E_z = 0$ taken from D2 at 4 K. b, Degree of circular polarization (DOCP) of the X_A^+ and X_A^-. The bright emission in the range of 1.5~ 1.6 eV corresponds to the momentum indirect trion/Fermi polaron. In contrast, the higher energy emission around 1.7eV corresponds to the momentum direct (K-K) intralayer trion/Fermi polaron. Both charged excitons X_I and X_A exhibit a redshift with increasing doping density.

Section 3. Effect of optical pumping on the oscillator strength of X_A^+

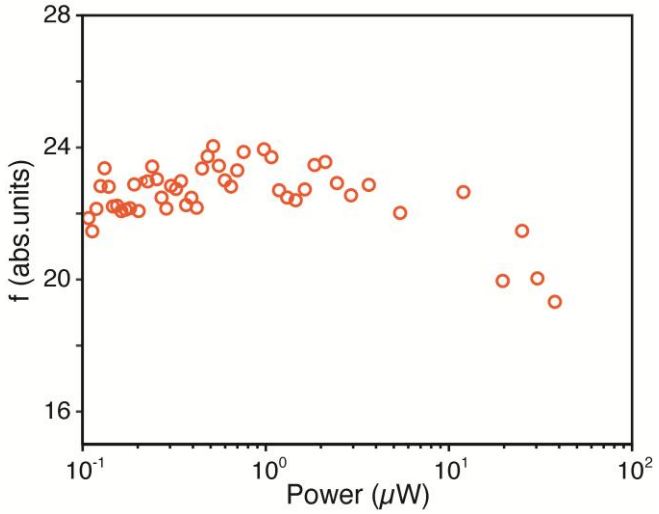

Figure S4 The oscillator strength of X_A^+, extracted from the reflectance spectra of sample **D3,** remains almost unchanged under low pump power and begins to decrease with increasing excitation power, when the blueshift becomes obvious.

Section 4. Optical nonlinearity under resonant excitation

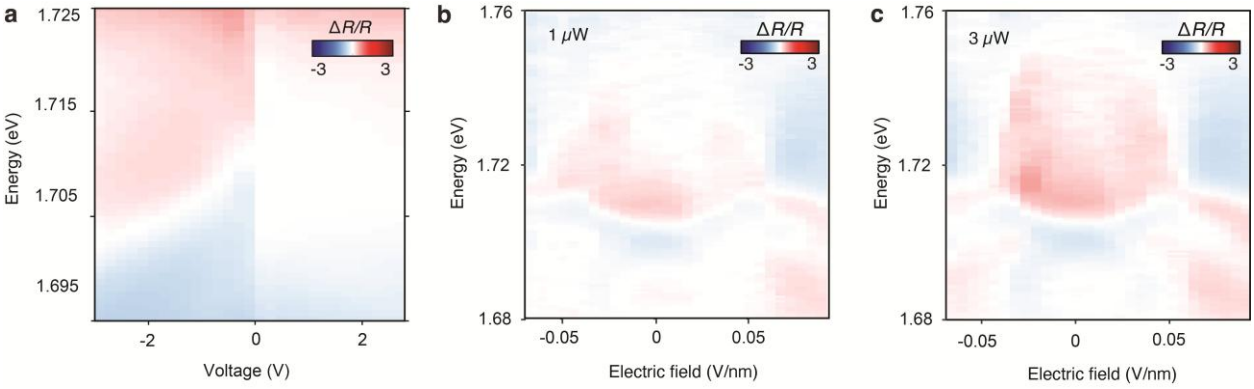

Figure S5. a, Relative change in the reflectance induced by 1 μW of resonant at resonant (718 to 730 nm) pulsed laser excitation under different doping. The color map is obtained by normalizing the reflectance change induced by the resonant excitation with respect to the reflectance without optical pumping, $\Delta R/R = \frac{R_{(1\,\mu W)}}{R_{(0.1\,\mu W)}} - 1$. The pulse has ~100 ps duration with a 40 MHz repetition rate. **b, c,** Reflectance change induced by a pulsed laser excitation power of 1 μW(**b**) and 3 μW(**c**), as a function of electric field, under hole doping. Under a small electric field, X_A^+ shows a blueshift, but it begins to redshift under excitation at a higher electric field. With increasing power, this transition point shifts to a lower electric field.

Section 5. Effect of pumping photon energy on nonlinearity

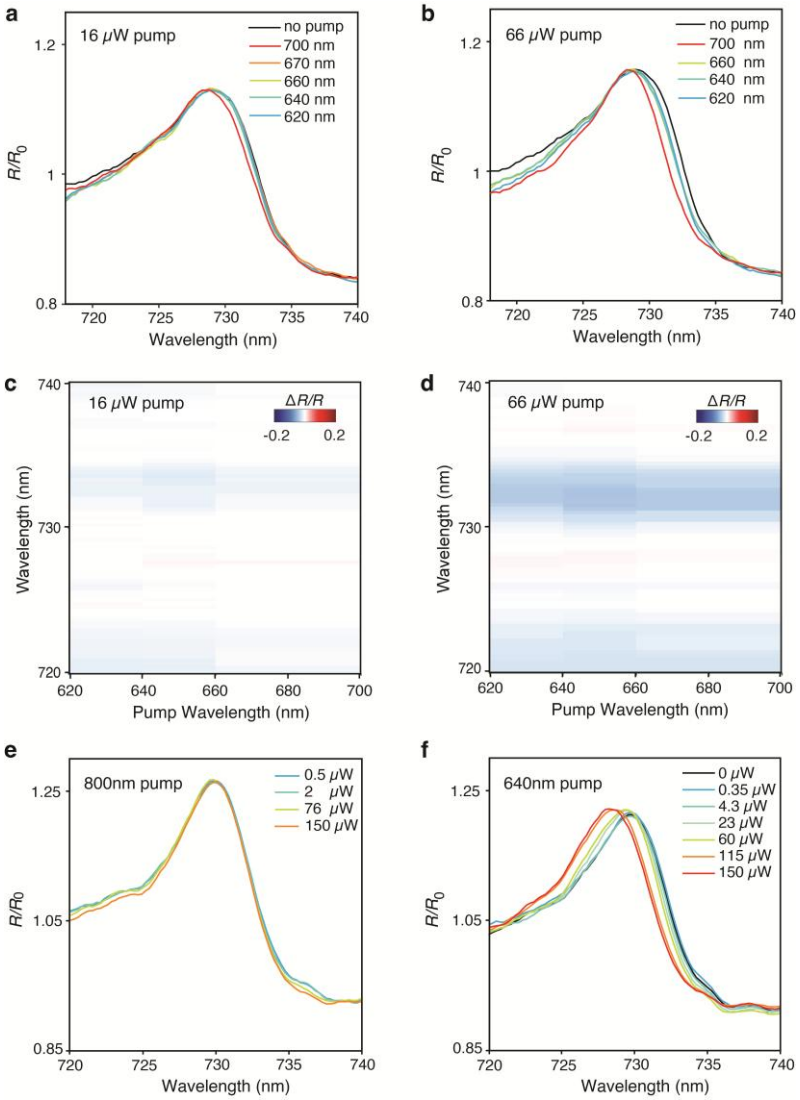

Figure S6 (a, b) Blueshift of X_A^+ under laser excitation at different center wavelengths (~10 nm spectral width) with a fixed pumping power at (a) 16 μW and (b) 66 μW. **(c, d)** The corresponding reflectance changes induced by optical pumping at different wavelengths show no significant wavelength dependence. **(e, f)** When exciting the system with photon energies below X_A^+, we did not observe significant blueshift (**e**), in contrast to higher energy excitation at 640nm (**f**). All data is acquired from device **D3**. We also note that the resonant excitation results in a much more pronounced blueshift (**Fig. S7**).

Section 6. Optical nonlinearity under different powers in various devices

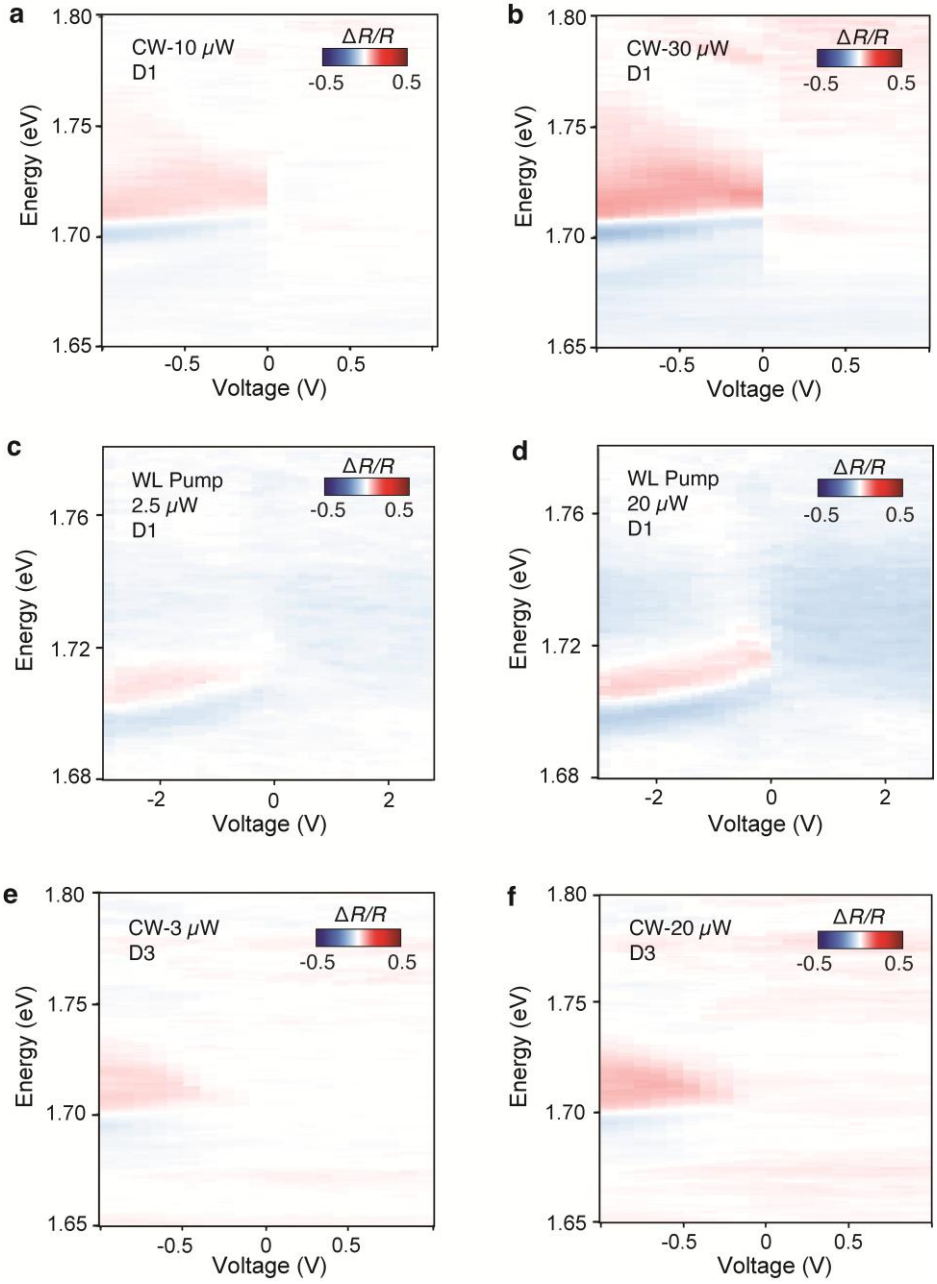

Figure S7 Relative change in the reflectance induced by optical pumping as a function of doping for various devices under different excitation conditions. We notice that the reflectance change is smooth near 0V, particularly at low excitation power. **(a)** 10 μW and high excitation power **(b)** 30 μW with 635 nm CW laser pumping for Device **D1. (c) 2.5** μW and **(d)** 20 μW 645nm pulsed laser excitation for device **D1. (e)** 10 μW and **(f)** 20 μW CW 635 nm laser pumping for Device **D3**.

Section 7. Effect of CW vs. pulsed excitation

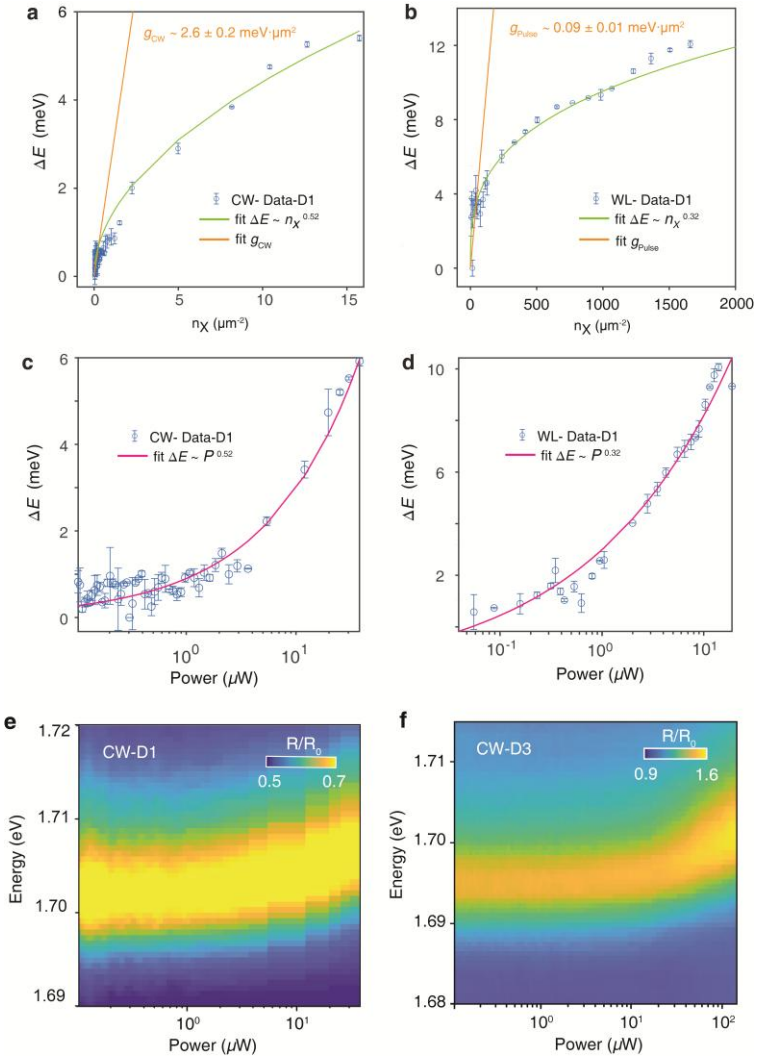

Figure S8 Analysis of power-dependent blueshift of X_A^+ under CW laser (a, c) and white laser excitation (b, d). a,b, Extraction of interaction strength g from (a) CW laser and (b) pulsed laser pumping induced X_A^+ blueshift vs. exciton density for **D1**. The exciton density is calculated from pump flux based on $n_X = P\alpha\tau/\hbar\omega$, where P is the pump power, α is the absorption coefficient, τ is the lifetime of the Fermi polaron, $\hbar\omega$ is the photon energy. The Fermi polaron lifetime is a few picoseconds, as measured in similar systems, and we use a value of 2 ps. The interaction strength is extracted from the linear fit of the $\Delta E - n_X$ curve in the low exciton density regime. The larger g values under CW excitation could be related to the complex relaxation dynamics of the exciton populations and an overestimation of exciton density under pulsed excitation. We also fit the blue shift amount as $\Delta E = a \cdot n_X{}^{(b)}$ over the entire data range. The fitting for CW laser and pulsed laser yields a coefficient of b as 0.52 with an R-square of 0.9516 for the CW laser and b of 0.32 with an R-square of 0.9317 for the pulsed laser, which shows a sublinear response for X_A^+ as polaron density. The hole doping density is kept at 8 x 10^{12} cm^{-2}. The error bars represent the variance of fitting peak energy. **c, d,** The same data as shown in **a, b**, plotted on a semilog scale,

to emphasize on the low power regime, with power as the x-axis. **e, f,** Power-dependent blueshift of X_A^+ under CW laser for **e,** device **D1** and **f,** device **D3**. The error bars represent the variance of fitting peak energy.

Section 8. Temperature dependence of X_A^+

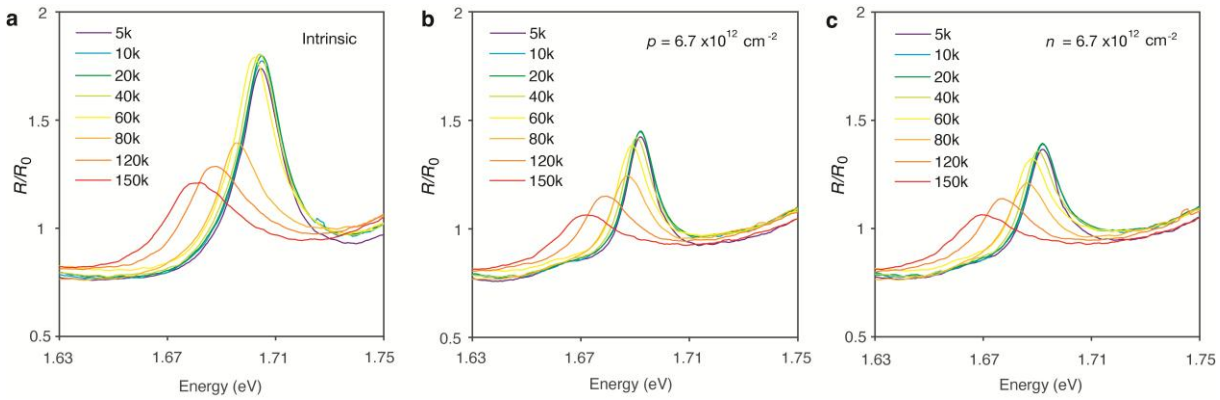

Figure S9 Temperature-dependent reflectance spectra of the trilayer under a constant doping density under zero electric field. In all cases, which include (**a**) intrinsic, (**b**) hole-doping, and (**c**) electron-doping, we observe strong redshift with increasing temperatures. Therefore, the observed nonlinearity, which corresponds to exciton blueshift, cannot be described as simple laser heating effects.

Section 9. Estimation of X_I density

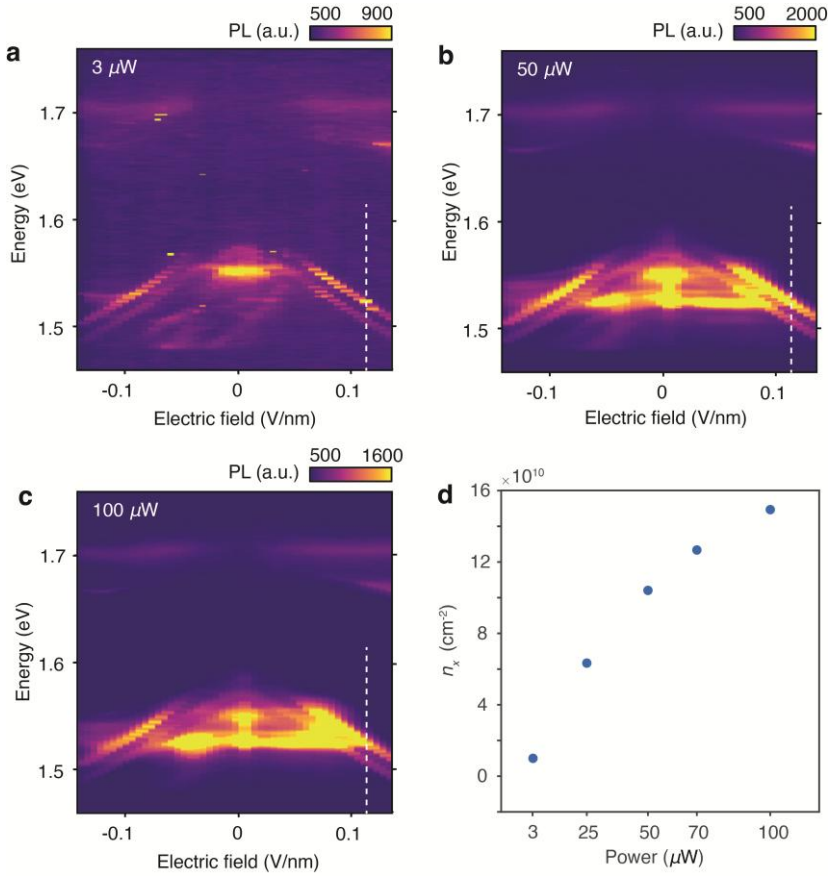

Figure S10 Estimation of X_I density as a function of pump power. a-c, Electric field-dependent PL map under different pump power (**a**) 3 μw, (**b**) 50 μw, (**c**)100 μw at the trilayer region. At an electric field of 0.12 V/nm, a maximum blue shift in a value of 3.3 meV of the X_I is observed. (**f**) X_I exciton density inferred from the above X_I blueshift under an applied electric field of 0.12 V/nm.

Section 10. Effect of circular polarization on Nonlinearity

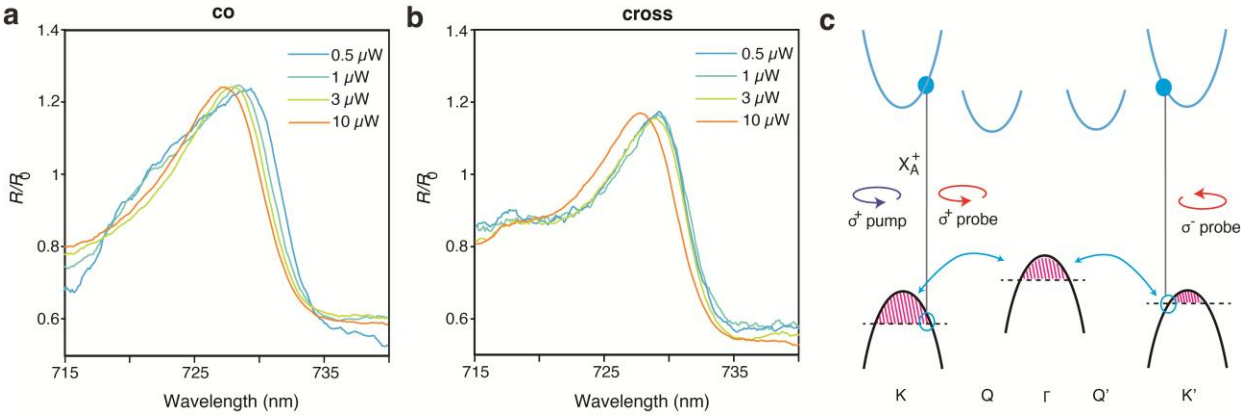

Figure S11 Valley-polarized holes under resonant circularly polarized excitation. (a, b) Power-dependent blueshift of X_A^+ under resonant pumping with **(a)** σ^+/σ^+ (pumping and probing K valley) and **(b)** σ^+/σ^- configuration (pumping K, while probing K' valley) when the sample is hole-doped. We observe a stronger blueshift of X_A^+ in **(a)**. We observe a stronger blueshift of XA+ in (a). In particular, we observe a ~1.3 nm blueshift under 3 μW pump when the pump and probe are co-polarized and no obvious shift in the cross-polarized case. Further increasing the pumping power to 10 μW leads to a blueshift in the cross-polarized setup, albeit still being smaller than the co-polarized case, which suggests the holes are partially polarized in K vs. K'. The data is acquired from device **D3**. **(c)** Nonequilibrium hole accumulation in K and K' valleys induced by selective valley pumping with a circularly polarized excitation. The resulting population imbalance between K and K' causes different amounts of blueshift in X_A^+ nonlinearity between the two valleys.

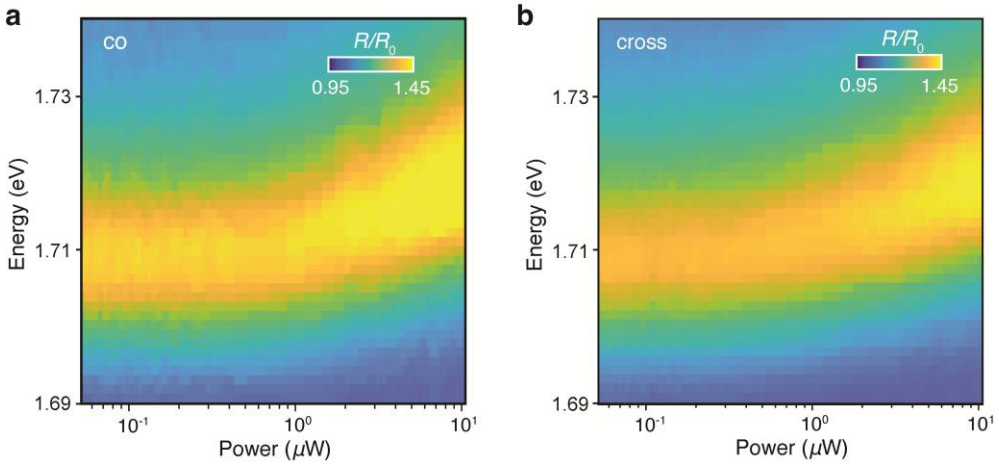

Figure S12 Non-resonant excitation with circular polarized polarization. Different from the resonant excitation case (**Fig. S12**), under non-resonant circularly polarized pump (635 nm), we observe similar magnitude of blueshift X_A^+ under **(a)** σ^+/σ^+ and **(b)** σ^+/σ^- configuration. This is

likely due to the breakdown of valley-selective optical selection rules far from the band edge as well as fast depolarization of excitons and electrons during the relaxation process.

Section 10. Electric-field tuning of Fermi polarons.

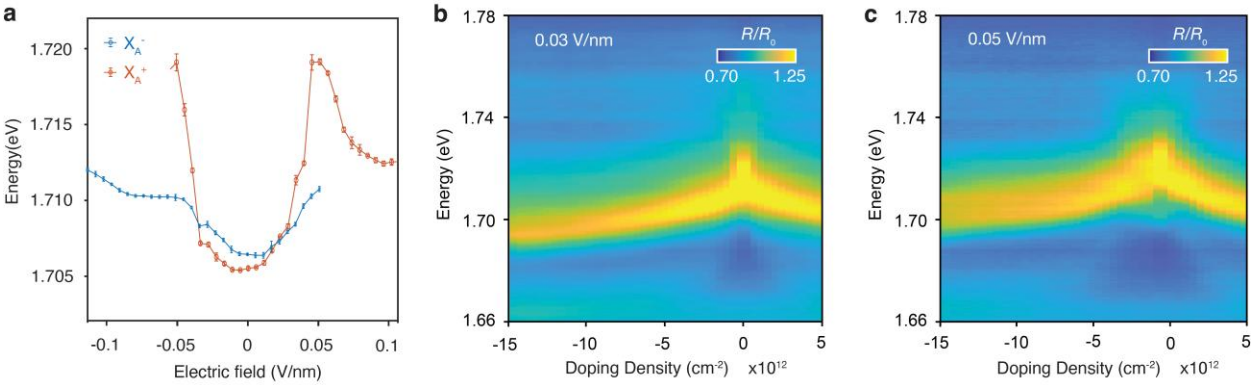

Figure S13 (a) Energy shift of X_A^- and X_A^+ with applied electric field with constant doping. The electron and hole doping densities are both kept at $4.9\times 10^{12} cm^{-2}$.The peak position is obtained by fitting the reflectance spectral with a Lorentzian model. The error bars represent the variance of fitting peak energy. **b,c,** Doping dependence of the intralayer Fermi polaron reflectance contrast R/R_0 in trilayer with applied (**a**) 0.03 V/nm, (**b**) 0.05 V/nm electric field. The negative doping density represents hole hole-doped side. An obvious blueshift and broadening of X_A^+ is observed on the hole side with an increasing electric field, corresponding to the additional phase space filling due to the population transfer from Γ to K valleys. Such a shift is much weaker on the electron side.

Section 11. Comparison of nonlinearity with previous work

Table S1

Here, we compare the amount of blueshift per pump power, which has important implications for low-power devices. Indeed, in our current work, much smaller pump power is needed to shift the absorption of excitons by a similar amount, in comparison with previous reports. This is related to the fact that the measured interaction strength g is much larger than previous reports and theoretical exchange/dipolar interactions. We also note that while one can observe a significant shift of interlayer excitons at relatively low power (Ref. [4, 5]), these species have negligible absorption because of long lifetime, as we discussed in the introduction of the paper.

	This work*	Ref. [1]	Ref. [2]	Ref. [3]	Ref. [4]	Ref. [5]
Species	Fermi Polaron	Hybridized Interlayer Exciton	Interlayer Exciton	2*s* Exciton Polariton	Interlayer Exciton	Interlayer Exciton
n_x (cm^{-2})	10^9	~$4*10^{12}$	~$2*10^{10}$	~$6*10^9$	$1.2*10^{11}$	~10^{12}
ΔE (meV)	6	~7	~2.2	1-2	~2	~22
Power ($\mu W/\mu m^2$)	37	$3.25*10^6$	1300	$3*10^4$	60	~300
System	Trilayer WSe_2	Bilayer MoS_2	Bilayer MoS_2	Monolayer WSe_2	Bilayer WSe_2	$MoSe_2$/ hBN/ WSe_2
Probe	Absorption	Absorption	Absorption	Absorption	PL	PL

References:

1. Datta, B. *et al.* Highly nonlinear dipolar exciton-polaritons in bilayer MoS2. *Nat. Commun.* **13**, 1–7 (2022).
2. Louca, C. *et al.* Interspecies exciton interactions lead to enhanced nonlinearity of dipolar excitons and polaritons in MoS2 homobilayers. *Nat. Commun.* **14**, 3818 (2023).
3. Gu, J. *et al.* Enhanced nonlinear interaction of polaritons via excitonic Rydberg states in monolayer WSe2. *Nat. Commun.* **12**, 2269 (2021).
4. Wang, Z., Chiu, Y.-H., Honz, K., Mak, K. F. & Shan, J. Electrical Tuning of Interlayer Exciton Gases in WSe_2 Bilayers. *Nano Lett.* **18**, 137–143 (2018).
5. Sun, Z. *et al.* Excitonic transport driven by repulsive dipolar interaction in a van der Waals heterostructure. *Nat. Photonics* **16**, 79–85 (2022).